
TrajLoom: Dense Future Trajectory Generation from Video

Zewei Zhang¹
zhanz561@mcmaster.ca

Jia Jun Cheng Xian^{2,3}
anthony@ece.ubc.ca

Kaiwen Liu^{2,3}
kaiwenliu@ece.ubc.ca

Ming Liang⁴
liangming.elgoog@gmail.com

Hang Chu⁴
hang.chu@warpengine.ai

Jun Chen¹
chenjun@mcmaster.ca

Renjie Liao^{2,3,5}
rjliao@ece.ubc.ca

¹ McMaster University ² University of British Columbia
³ Vector Institute ⁴ Viggle AI ⁵ Canada CIFAR AI Chair

Abstract

Predicting future motion is crucial in video understanding and controllable video generation. Dense point trajectories are a compact, expressive motion representation, but modeling their future evolution from observed video remains challenging. We propose a framework that predicts future trajectories and visibility from past trajectories and video context. Our method has three components: (1) Grid-Anchor Offset Encoding, which reduces location-dependent bias by representing each point as an offset from its pixel-center anchor; (2) TrajLoom-VAE, which learns a compact spatiotemporal latent space for dense trajectories with masked reconstruction and a spatiotemporal consistency regularizer; and (3) TrajLoom-Flow, which generates future trajectories in latent space via flow matching, with boundary cues and on-policy K -step fine-tuning for stable sampling. We also introduce TrajLoomBench, a unified benchmark spanning real and synthetic videos with a standardized setup aligned with video-generation benchmarks. Compared with state-of-the-art methods, our approach extends the prediction horizon from 24 to 81 frames while improving motion realism and stability across datasets. The predicted trajectories directly support downstream video generation and editing. We released code, model checkpoints, and datasets at <https://trajloom.github.io/>.

1 Introduction

Motion is central to video and carries information beyond static appearance [33]. Recent video generation and editing systems rely on motion cues—including camera control, optical flow, and trajectory guidance—to shape temporal dynamics [12, 3, 40, 5, 7]. Point trajectories are a flexible motion representation. Modern trackers can recover dense trajectories with long-range correspondences and occlusion patterns [15, 17, 38, 8]. This motivates a key question: given trajectories in a fixed history window, how can we predict their future positions and visibility over a future horizon?

Trajectory forecasting methods model future motion directly in trajectory space [36, 41, 1, 42]. However, future motion is inherently uncertain and multimodal, making deterministic prediction insufficient. A recent method, *What Happens Next?* (WHN) [2], formulates trajectory anticipation as a generative task and is primarily conditioned on appearance cues in a given image and possibly text prompts. However, appearance-only conditioning overlooks explicit motion history. Observed

trajectories already encode current dynamics and strongly constrain plausible futures. This motivates future-trajectory generation conditioned on trajectory and video history. The main challenges are preserving temporal stability and local coherence across forecast windows in diverse real-world videos.

In contrast to image-conditioned trajectory generators, we forecast from observed trajectory and video history. This conditioning captures ongoing dynamics and differs from WHN-style appearance-driven generation, which mainly depends on image content [2]. A central design question is how to represent dense trajectories for learning. Most methods use *absolute* image coordinates [2], which couple motion with global position and induce location-dependent statistics. We instead propose Grid-Anchor Offset Encoding, which represents each trajectory as a displacement from a fixed pixel-center anchor. Absolute coordinates are recovered by adding anchors back. This offset-based parameterization emphasizes motion rather than location and provides a stable foundation for latent generative modeling.

Even with Grid-Anchor Offset Encoding, forecasting dense trajectory fields remains high-dimensional. We first learn TrajLoom-VAE, a variational autoencoder (VAE) [20] that maps trajectory segments to compact spatiotemporal tokens and reconstructs dense tracks. To preserve motion structure, TrajLoom-VAE applies a spatiotemporal consistency regularizer that aligns velocities with local neighbors. We then generate future motion in this latent space using TrajLoom-Flow, a rectified-flow model conditioned on observed trajectories and video that predicts the full future window [22, 24]. Lightweight boundary cues enforce continuity with observed history. Because training uses constructed interpolation states whereas inference queries self-visited ODE states, we further use on-policy K -step fine-tuning to reduce this mismatch.

For evaluation, we introduce TrajLoomBench, a unified benchmark spanning real and synthetic videos with standardized setups (e.g., resolution and horizon) as common video generation benchmarks [8, 35, 13, 21]. Compared with WHN [2], our method improves motion realism, temporal consistency, and stability in both quantitative and qualitative evaluations. We also show that the predicted trajectories effectively guide motion-controlled video generation and editing [37, 5].

We summarize our main contributions as follows.

1. **Trajectory encoding:** Grid-Anchor Offset Encoding, which represents each point as an offset from a fixed grid anchor to reduce location-dependent bias in dense trajectory prediction.
2. **Latent trajectory generation:** A generative framework that combines (i) TrajLoom-VAE, a VAE with masked reconstruction and spatiotemporal regularization for compact, structured trajectory latents, and (ii) TrajLoom-Flow, a rectified-flow generator conditioned on observed trajectories and video, with boundary cues and on-policy K -step fine-tuning for stable sampling over extended forecast windows.
3. **Benchmark and results:** TrajLoomBench, a unified benchmark for dense trajectory forecasting in natural videos. Our approach achieves state-of-the-art performance and provides a strong foundation for downstream applications such as motion-controlled video generation and editing.

2 Related Works

Trajectories for motion anticipation. Modern tracking-any-point methods track long-range point trajectories (with visibility/occlusion) in unconstrained videos, enabling dense correspondence under large motion and occlusions [8–10, 17, 38, 15, 14]. Recent datasets and training pipelines further scale tracking quality and diversity, e.g., PointOdyssey for long synthetic sequences and BootsTAP for leveraging unlabeled real video [47, 10]. Given an observed history window of tracks and visibility, *trajectory prediction* forecasts future positions directly in trajectory space. It has been used for forecasting, planning, and imitation in robotics and action reasoning [36, 35, 41, 1, 42]. Most approaches remain regression-based and can average over multiple plausible futures, becoming conservative and accumulating drift over long horizons. This motivates formulating future motion as generative. *What Happens Next?* (WHN) samples dense future trajectories from appearance cues like image or text, instead of predicting a single deterministic continuation [2]. Our work follows this generative direction but conditions on the observed motion history, leveraging constraints already present in tracked trajectories.

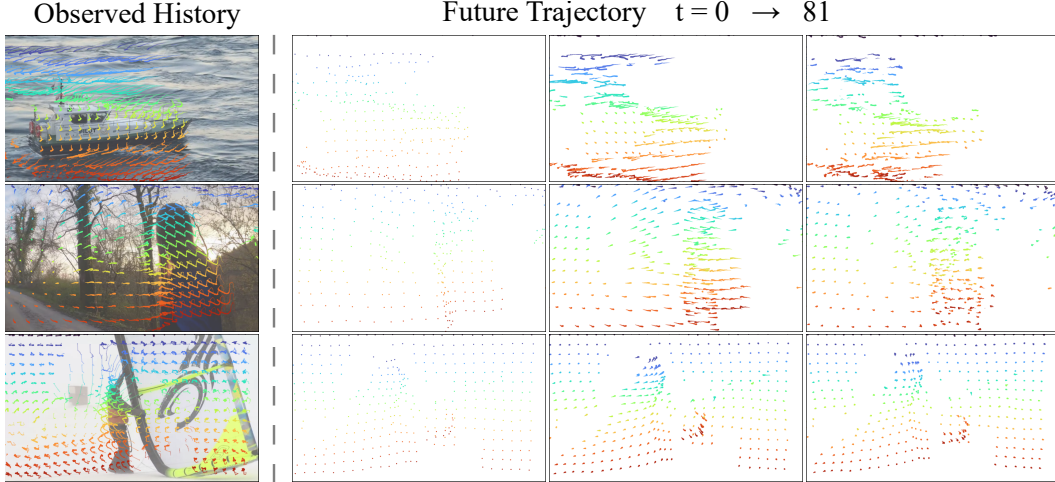


Figure 1: For each sequence, the model observes an 81-frame history (left) and predicts future trajectories for the next 81 frames (right). Predicted trajectories are shown at three times: early, middle, and final. Colors show the spatial order of query points.

Motion-guided generation and editing. Controllable video generation often incorporates explicit motion controls such as optical flow, camera trajectories, or point tracks to guide temporal dynamics in diffusion-based models [40, 3, 12, 39]. Trajectory-conditioned methods use sparse or dense tracks as a low-level interface for directing object motion, as exemplified by DragNUWA, MagicMotion, Tora, and SG-I2V [43, 21, 46, 27]. Wan-Move is particularly relevant to our applications. Built on the Wan image-to-video backbone, it employs latent trajectory guidance that propagates information along dense point trajectories, enabling direct point-level motion control [5, 37]. Interactive editing similarly uses sparse point constraints to manipulate deformation and motion. These range from DragGAN and DragDiffusion to video drag methods such as DragVideo [28, 32, 45, 7]. Our future-trajectory generator complements these controllers. We adopt Wan-Move because it consumes dense trajectories *directly*, allowing our predicted tracks to integrate without additional motion representations [5].

3 TrajLoom: Dense Future Trajectory Generation

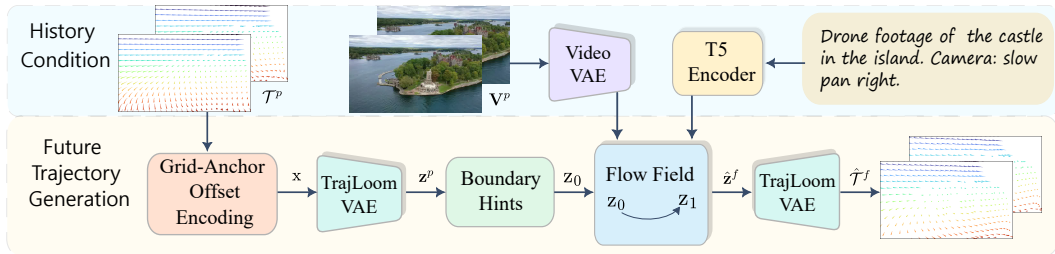
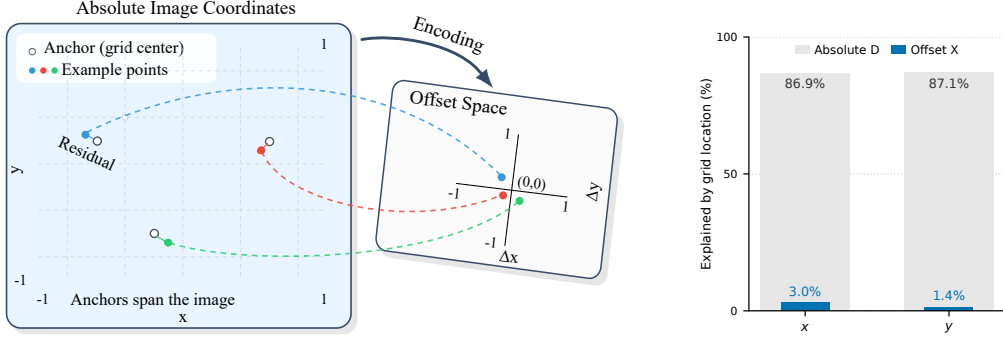


Figure 2: **Overview of our pipeline.** Given observed trajectories \mathcal{T}^p , we rasterize and encode them with Grid-Anchor Offset Encoding into a dense offset field, then compress with TrajLoom-VAE into history latents \mathbf{z}^p . Conditioned on \mathbf{z}^p and video features, TrajLoom-Flow generates future latents via rectified-flow integration with boundary hints, which are decoded by TrajLoom-VAE into future trajectories $\hat{\mathcal{T}}^f$.

We study future-motion generation from observed history in a video clip. A video is denoted as $\mathbf{V} \in \mathbb{R}^{T \times H \times W \times 3}$, where T is the total number of frames, and each frame has a spatial resolution of $H \times W$. Motion is represented as a set of N trajectories, $\mathcal{T} = \{\tau_n\}_{n=1}^N$, where each trajectory $\tau_n = \{(x_{n,t}, y_{n,t})\}_{t=0}^{T-1}$ tracks one reference 2D point through time. At each frame t , the location of the point is $(x_{n,t}, y_{n,t})$, accompanied by a visibility indicator $v_{n,t} \in \{0, 1\}$. For clarity, we split each clip into a past history window of length T_p and a future window of length T_f , where



(a) **Grid-Anchor Offset Encoding.** We encode trajectories as displacements from pixel-center anchors: instead of absolute coordinates (left), each point is given by its offset $(\Delta x, \Delta y)$ from its local anchor (right), producing a zero-centered, location-consistent representation.

(b) Variance explained by grid location for absolute and offset coordinates. We measure coordinate variance attributable to grid position using time-averaged coordinates at each grid cell.

Figure 3: Grid-Anchor Offset Encoding converts absolute trajectories into offset space, reducing the bias of absolute coordinates.

$T_p + T_f = T$. Thus, \mathbf{V} is divided as $\mathbf{V} = (\mathbf{V}^p, \mathbf{V}^f)$. Each trajectory τ_n is similarly partitioned into a history segment, $\tau_n^p = \{(x_{n,t}, y_{n,t})\}_{t=0}^{T_p-1}$, and a future segment, $\tau_n^f = \{(x_{n,t}, y_{n,t})\}_{t=T_p}^{T-1}$. Visibility indicators are split in the same manner. Given the observed history trajectories $\mathcal{T}^p = \{\tau_n^p\}_{n=1}^N$, their corresponding visibility indicators, the history video clip \mathbf{V}^p , and a text caption, our goal is to generate the corresponding future trajectories $\hat{\mathcal{T}}^f$.

Our pipeline has three stages: Grid-Anchor Offset Encoding densifies sparse trajectories into grid-anchored offsets (Section 3.1); TrajLoom-VAE compresses dense fields into compact spatiotemporal latents with masked reconstruction and spatiotemporal regularization (Section 3.2); and TrajLoom-Flow jointly predicts future latents via a history-conditioned rectified flow, then decodes them into trajectories (Section 3.3). To reduce train-test mismatch from ODE integration [4], we further apply on-policy K -step fine-tuning.

3.1 Grid-Anchor Offset Encoding

Starting from trajectories $\mathcal{T} = \{\tau_n\}_{n=1}^N$, Grid-Anchor Offset Encoding constructs a dense trajectory representation on the video grid. Grid-Anchor Offset Encoding represents each pixel by its displacement from a local pixel-center anchor, rather than by absolute coordinates. This yields offsets that are consistent and comparable across grid locations.

Concretely, trajectories are extracted from a stride- s grid. Let $H_c = H/s$ and $W_c = W/s$ so that $N = H_c W_c$. Rasterization produces (i) a dense absolute coordinate field $\mathbf{D} \in \mathbb{R}^{T \times H \times W \times 2}$ and (ii) a dense visibility mask $\mathbf{M} \in \{0, 1\}^{T \times H \times W}$. For a pixel location $p = (h, w)$, the corresponding coarse-grid trajectory index is $\pi(h, w) = \lfloor h/s \rfloor W_c + \lfloor w/s \rfloor + 1$ and the dense fields are defined by $\mathbf{D}(t, h, w) = (x_{\pi(h,w),t}, y_{\pi(h,w),t})$ and the mask is $\mathbf{M}(t, h, w) = v_{\pi(h,w),t}$. By construction, \mathbf{D} and \mathbf{M} are piecewise constant within each $s \times s$ stride cell. All coordinates are represented in a normalized image coordinate system.

For each pixel p at location (h, w) in the dense field, we define its normalized pixel-center anchor $\mathbf{G}(p) \in \mathbb{R}^2$, where $\mathbf{G}(p) = \left[2 \frac{w+\frac{1}{2}}{W} - 1, 2 \frac{h+\frac{1}{2}}{H} - 1 \right]^\top$. The offset-encoded trajectory field is then $\mathbf{X}(t, p) = \mathbf{D}(t, p) - \mathbf{G}(p)$. From now on, the offset field \mathbf{X} , together with the visibility mask \mathbf{M} , serves as the trajectory representation. Absolute coordinates can be recovered from this representation.

We validate Grid-Anchor Offset Encoding by comparing coordinate variance under absolute and relative representations. With absolute coordinates \mathbf{D} , trajectory variance is dominated by grid location: points from different grid cells are centered at different image positions, so the overall

variance is large even when local motion is similar. To quantify this effect, we compute the fraction of coordinate variance explained by grid location, using a visibility-weighted time-averaged coordinate at each grid position as the location baseline. Figure 3b shows that this explained variance is high for absolute coordinates but much lower for relative offsets. Using offsets $\mathbf{X} = \mathbf{D} - \mathbf{G}$ removes most location-driven variance and yields a more uniform representation focused on local displacement. More details can be found in Appendix B.1.

3.2 TrajLoom-VAE

Modeling future motion directly in dense trajectory-field space is high-dimensional. To obtain a compact representation for generative modeling, we learn a variational autoencoder (VAE) in the latent space. TrajLoom-VAE is trained on temporal segments \mathbf{x} from the offset-encoded trajectory field \mathbf{X} (Section 3.1) and the corresponding visibility mask \mathbf{m} . Given a segment \mathbf{x} , the encoder defines an approximate posterior $q_\phi(\mathbf{z} | \mathbf{x})$, and the decoder reconstructs it as $\hat{\mathbf{x}} = \psi(\mathbf{z})$.

A masked pointwise reconstruction loss encourages $\hat{\mathbf{x}}$ to match \mathbf{x} at visible locations, but it does not directly model temporal evolution or local relative motion. As a result, reconstructions with reconstruction error alone still show temporal jitter or local spatial inconsistency (see Appendix B.2). To enforce temporal smoothness and local coherence, we propose a *spatiotemporal consistency regularizer* that matches (i) temporal velocities and (ii) multiscale spatial neighbor relations between the target segment \mathbf{x} and reconstruction $\hat{\mathbf{x}}$.

3.2.1 Spatiotemporal consistency regularizer.

The regularizer combines a temporal velocity term and a multiscale spatial neighbor term. Let Ω denote the set of spacetime indices (t, p) within a segment window. The trajectory value at (t, p) is $\mathbf{x}(t, p) \in \mathbb{R}^2$, and the corresponding visibility is $\mathbf{m}(t, p) \in \{0, 1\}$. All consistency terms are computed only on valid, visible pairs and are normalized by the number of such pairs so that the loss scale does not depend on how many points are visible.

We discourage the frame-to-frame jittering by the following loss,

$$L_{\text{temporal}} = \frac{1}{\sum_{(t,p) \in \Omega} \mathbf{m}_{\text{pair}}(t,p)} \sum_{(t,p) \in \Omega} \mathbf{m}_{\text{pair}}(t,p) \|\Delta_i \hat{\mathbf{x}}(t,p) - \Delta_i \mathbf{x}(t,p)\|_1, \quad (1)$$

where $\Delta_i \mathbf{x}(t,p) = \mathbf{x}(t,p) - \mathbf{x}(t-1,p)$, $\Delta_i \hat{\mathbf{x}}(t,p) = \hat{\mathbf{x}}(t,p) - \hat{\mathbf{x}}(t-1,p)$, and $\mathbf{m}_{\text{pair}}(t,p) = \mathbf{m}(t,p)\mathbf{m}(t-1,p)$. Basically, it matches the temporal consistency between the reconstruction and the ground truth for locations that are visible.

To preserve spatial consistency, we additionally match relative motion among neighboring locations. Let \mathcal{S} be a set of horizontal/vertical offsets at multi-hop distances. For each neighboring location $\delta \in \mathcal{S}$, we define $\Delta_\delta \mathbf{x}(t,p) = \mathbf{x}(t,p+\delta) - \mathbf{x}(t,p)$ and $\Delta_\delta \hat{\mathbf{x}}(t,p) = \hat{\mathbf{x}}(t,p+\delta) - \hat{\mathbf{x}}(t,p)$, and introduce the following loss,

$$L_{\text{spatial}} = \frac{1}{\sum_{\delta \in \mathcal{S}} \alpha_\delta} \sum_{\delta \in \mathcal{S}} \alpha_\delta \frac{\sum_{(t,p) \in \Omega} \mathbf{m}_\delta(t,p) \|\Delta_\delta \hat{\mathbf{x}}(t,p) - \Delta_\delta \mathbf{x}(t,p)\|_1}{\sum_{(t,p) \in \Omega} \mathbf{m}_\delta(t,p)}. \quad (2)$$

The loss is only activated when both neighboring locations are visible since $\mathbf{m}_\delta(t,p) = \mathbf{m}(t,p)\mathbf{m}(t,p+\delta)$. Each neighbor is weighted by α_δ and then normalized by the sum over the neighborhood. The set $\mathcal{S} = \{1, 2, 4\}$ determines the hop distances used, with the corresponding Δ_δ values of 1, 0.5, and 0.25. We scale down the α_δ by the neighborhood distance; the larger the distance δ , the smaller α_δ . This makes the spatial loss L_{spatial} focus more on local motion, since the global motion is captured by the reconstruction loss.

Therefore, the full spatiotemporal consistency regularizer is,

$$L_{\text{st}} = \lambda_{\text{temporal}} L_{\text{temporal}} + \lambda_{\text{spatial}} L_{\text{spatial}}, \quad (3)$$

where $\lambda_{\text{temporal}}$ and λ_{spatial} are weighting coefficients.

Appendix B.2 and Figure 7 provide a toy example showing why pointwise reconstruction alone is insufficient and how the consistency regularizer separates smooth from jittery solutions.

3.2.2 Training objective.

The reconstruction loss of our VAE is as follows,

$$L_{\text{rec}} = \sum_{(t,p) \in \Omega} w(t,p) \rho(\hat{\mathbf{x}}(t,p) - \mathbf{x}(t,p)), \quad (4)$$

where the normalized mask $w(t,p) = \mathbf{m}(t,p) / \sum_{(j,q) \in \Omega} \mathbf{m}(j,q)$ ensures that we only consider visible locations. ρ is the Huber loss [16].

We train TrajLoom-VAE by minimizing reconstruction error, the KL divergence, and the spatiotemporal consistency regularizer,

$$L_{\text{vae}} = \mathbb{E}_{q_\phi(\mathbf{z}|\mathbf{x})} [L_{\text{rec}} + L_{\text{st}}] + \beta D_{\text{KL}}(q_\phi(\mathbf{z} | \mathbf{x}) \| \mathcal{N}(\mathbf{0}, \mathbf{I})), \quad (5)$$

where β is the weighting of the KL term. In practice, we set $\beta = 5 \times 10^{-5}$, $\lambda_{\text{temporal}}$ as 0.1, and λ_{spatial} as 0.2 for the spatiotemporal consistency regularizer.

3.3 TrajLoom-Flow

We generate future motion in the latent space learned by TrajLoom-VAE. Given a history segment \mathbf{x}^p and a future segment \mathbf{x}^f (both from the offset field \mathbf{X}), we obtain their latent representations with the frozen VAE encoder. We use the posterior mean as a deterministic encoding:

$$\mathbf{z}^p = \mathbb{E}_{q_\phi(\mathbf{z}|\mathbf{x}^p)}[\mathbf{z}], \quad \mathbf{z}^f = \mathbb{E}_{q_\phi(\mathbf{z}|\mathbf{x}^f)}[\mathbf{z}]. \quad (6)$$

TrajLoom-Flow models the conditional distribution of future latents given observed history and predicts the full future window jointly.

To keep predictions consistent with observed motion, we summarize all conditioning signals as \mathbf{c} . In our setting, \mathbf{c} includes history trajectory latents \mathbf{z}^p , history visibility, and history-video features. The generator is a latent flow matching model, parameterized by a conditional velocity field $v_\theta(\mathbf{z}_t, t, \mathbf{c})$.

3.3.1 Boundary hints.

Because we generate the entire future window jointly, we provide explicit boundary information so the model can align future predictions with the observed past. We use two lightweight mechanisms: (i) a boundary-anchored initialization of \mathbf{z}_0 , and (ii) token-aligned fusion of history latents into the query stream.

Let $\Lambda = \{(k, n)\}$ index latent tokens, where k denotes a latent time index and n denotes a spatial token index, and let $\mathbf{z}(k, n) \in \mathbb{R}^C$ denote a token. Denoting by $\mathbf{z}(-1, n)$ the latent at the last history time step, we initialize the source state by repeating this boundary latent across the future horizon and adding Gaussian noise:

$$\mathbf{z}_0(k, n) = \mathbf{z}(-1, n) + \sigma_0 \boldsymbol{\eta}(k, n), \quad \boldsymbol{\eta} \sim \mathcal{N}(\mathbf{0}, \mathbf{I}), \quad (7)$$

where σ_0 controls the noise scale. In practice, we apply this anchoring at $k = 0$.

Beyond conditioning through \mathbf{c} , we inject history latents \mathbf{z}^p into the velocity network through a small token-aligned fusion module, providing a direct boundary cue. More details are in Appendix E.1 and the ablation study in Appendix D.3.

3.3.2 Flow matching.

To model a distribution over future latents without autoregressive rollout, we adopt rectified flow [22, 24] and learn a conditional latent velocity field. Denote the future target as $\mathbf{z}_1 = \mathbf{z}^f$, and let \mathbf{z}_0 be the history-conditioned source state. For flow time $t \in [0, 1]$, an intermediate state is

$$\mathbf{z}_t = (1-t)\mathbf{z}_0 + t\mathbf{z}_1 + \sigma \boldsymbol{\epsilon}, \quad \boldsymbol{\epsilon} \sim \mathcal{N}(\mathbf{0}, \mathbf{I}), \quad (8)$$

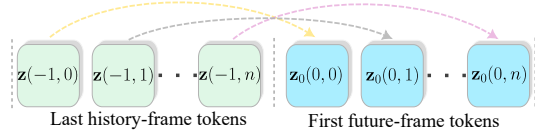


Figure 4: We initialize \mathbf{z}_0 from scaled Gaussian noise, then add each last history token $\mathbf{z}(-1, n)$ to the first future token $\mathbf{z}_0(0, n)$.

and the model predicts a conditional velocity field $v_\theta(\mathbf{z}_t, t, \mathbf{c})$. Under linear interpolation, the target velocity is $u_t = \mathbf{z}_1 - \mathbf{z}_0$, and training matches v_θ to u_t .

To emphasize visible future regions, we obtain a token-level weight $\mathbf{m}^{\text{tok}}(k, n) \in [0, 1]$ by pooling the future visibility mask onto the VAE token grid. We define normalized token weights as $w_\Lambda(k, n) = \mathbf{m}^{\text{tok}}(k, n) / \sum_{(j, q) \in \Lambda} \mathbf{m}^{\text{tok}}(j, q)$. The resulting visibility-weighted flow-matching loss is

$$L_{\text{fm}} = \mathbb{E}_{t, \epsilon} \left[\frac{1}{C} \sum_{(k, n) \in \Lambda} w_\Lambda(k, n) \|v_\theta(\mathbf{z}_t, t, \mathbf{c})(k, n) - u_t(k, n)\|_2^2 \right], \quad (9)$$

where C denotes the number of latent channels in \mathbf{z} .

3.3.3 On-policy fine-tuning.

Flow matching trains v_θ using interpolated states \mathbf{z}_t , while sampling evaluates v_θ on states produced by integrating the learned ODE. This mismatch can cause drift because the model is queried off the training path. We therefore apply an on-policy K -step rollout loss to fine-tune v_θ on its own visited states.

Let $\varepsilon = t_0 < t_1 < \dots < t_K = 1 - \varepsilon$ be an increasing time grid and set $\tilde{\mathbf{z}}_0 = \mathbf{z}_0$. A detached forward-Euler rollout generates visited states

$$\tilde{\mathbf{z}}_{i+1} = \tilde{\mathbf{z}}_i + (t_{i+1} - t_i) \text{sg}[v_\theta(\tilde{\mathbf{z}}_i, t_i, \mathbf{c})], \quad i = 0, \dots, K-1. \quad (10)$$

Denote $\mathbf{v}_i = v_\theta(\tilde{\mathbf{z}}_i, t_i, \mathbf{c})$. Endpoint-consistent velocity targets are

$$\mathbf{v}_i^{(1)} = \frac{\mathbf{z}_1 - \tilde{\mathbf{z}}_i}{1 - t_i}, \quad \mathbf{v}_i^{(0)} = \frac{\tilde{\mathbf{z}}_i - \mathbf{z}_0}{t_i}. \quad (11)$$

The on-policy rollout loss is defined as,

$$L_{\text{k-step}} = \frac{1}{K} \sum_{i=0}^{K-1} \left(w_1 \|\mathbf{v}_i - \mathbf{v}_i^{(1)}\|_{w_\Lambda}^2 + w_0 \|\mathbf{v}_i - \mathbf{v}_i^{(0)}\|_{w_\Lambda}^2 \right), \quad (12)$$

where $\|f\|_{w_\Lambda}^2 = \frac{1}{C} \sum_{(k, n) \in \Lambda} w_\Lambda(k, n) \|f(k, n)\|_2^2$. We further introduce a simple endpoint-consistency term to stabilize implied endpoints along the rollout,

$$L_{\text{cons}} = \frac{1}{K-1} \sum_{i=1}^{K-1} \left(\|\hat{\mathbf{z}}_i^{(1)} - \text{sg}[\hat{\mathbf{z}}_{i-1}^{(1)}]\|_{w_\Lambda}^2 + \|\hat{\mathbf{z}}_i^{(0)} - \text{sg}[\hat{\mathbf{z}}_{i-1}^{(0)}]\|_{w_\Lambda}^2 \right), \quad (13)$$

where $\hat{\mathbf{z}}_i^{(1)} = \tilde{\mathbf{z}}_i + (1 - t_i)\mathbf{v}_i$ and $\hat{\mathbf{z}}_i^{(0)} = \tilde{\mathbf{z}}_i - t_i\mathbf{v}_i$. The final loss is,

$$L = L_{\text{fm}} + \lambda_{\text{k-step}} \left(L_{\text{k-step}} + \gamma L_{\text{cons}} \right). \quad (14)$$

In practice, we apply this loss on a small sub-batch to limit overhead, and use small $\lambda_{\text{k-step}}$ and γ to stabilize training. More details are in Appendix A.3.

3.3.4 Sampling.

At inference, we obtain future latents by integrating the learned rectified-flow ODE from the history-conditioned source state. We take the final state as the generated future latent $\hat{\mathbf{z}}^f = \mathbf{z}(1)$. Finally, $\hat{\mathbf{z}}^f$ is decoded using the frozen TrajLoom-VAE decoder to obtain future dense trajectories.

4 Experiments

We evaluate both components of our framework: TrajLoom-VAE for trajectory reconstruction and TrajLoom-Flow for future trajectory generation.

4.1 Implementation Details

4.1.1 Baseline.

We compare against WHN (L), the largest variant of WHN [2], a state-of-the-art image-conditioned dense trajectory generator.

4.1.2 Trajectory extraction.

Our framework is trained and evaluated on dense trajectory fields \mathbf{X} and visibility masks \mathbf{M} (Section 3). Each video is converted to (\mathbf{X}, \mathbf{M}) via dense point tracking followed by rasterization. For all datasets, we extract dense long-range trajectories \mathcal{T} with AllTracker [15], using the first frame as reference and a stride-32 grid, for both training and evaluation.

4.1.3 Training dataset.

Training uses MagicData [21], a motion-focused text–video dataset with about 23k video–caption pairs. We apply standard filtering by aspect ratio, resolution, and clip length for consistency. Following WAN [37], videos are processed at 480p, and clips shorter than 162 frames are removed. After filtering, 16k videos remain; we use the first 162 frames of each video to match our forecasting window. We split these samples 90%/10% for training and validation.

4.1.4 Benchmark.

Evaluation uses TrajLoomBench, introduced in this work. It includes real and synthetic videos aggregated from existing datasets, covers diverse dense-forecasting scenarios, and uses MagicData validation. We then apply a unified resolution, temporal length, and preprocessing pipeline for fair comparison.

(i) *Real-world sources.* TAP-Vid evaluation sources [8] are reconstructed from raw videos. Specifically, TAP-Vid-Kinetics is constructed from YouTube IDs and temporal segments from the Kinetics-700 validation set [18], and RoboTAP [35] is provided in the same point-track annotation format as other TAP-Vid-style datasets. Instead of using TAP-Vid resized videos, we re-extract all videos at the target resolution and convert them into fixed-length temporal windows to match the forecasting horizon.

(ii) *Synthetic sources.* In its original work, WHN (L) [2] is trained and evaluated on a Kubric variant (MOVi-A) [13], enabling direct comparison on this dataset. Kubric is also a primary synthetic source in TAP-Vid [8]. For comparability, we follow the same MOVi-A configuration as WHN and re-render longer videos when needed.

4.1.5 Model and training.

Following WHN [2], we use a DiT backbone [29], specifically Latte [26], for both TrajLoom-VAE and TrajLoom-Flow. TrajLoom-VAE uses 16 blocks, 8 attention heads, 512 hidden dimensions, and 16 latent channels, plus a temporal convolution layer for temporal downsampling. TrajLoom-Flow follows the WHN (L) scale: 16 blocks, 12 heads, and 768 hidden dimensions. We train with AdamW [19, 25] at learning rate 6×10^{-5} , and use 1×10^{-5} for on-policy fine-tuning. Additional architecture and hyperparameter details are provided in Appendix A.

4.1.6 Evaluation Metrics.

We report evaluation metrics for (i) reconstruction fidelity of TrajLoom-VAE and (ii) motion quality of TrajLoom-Flow. For the generator, we use FVMD [23] to evaluate motion realism and temporal consistency, and two reference-free diagnostics (FlowSmoothTV and DivCurlEnergy) to assess trajectory quality. For the VAE, we report visibility-masked endpoint error (VEPE) as the reconstruction metric.

(i) *Fréchet Video Motion Distance (FVMD).* FVMD [23] uses Fréchet distance to compare motion-feature distributions derived from point trajectories. Unless noted otherwise, we use the official setting (clip length 16, stride 1) and restrict feature extraction to visible points via the trajectory visibility mask. Standard FVMD uses short 16-frame clips to capture fine-grained motion. For long-horizon forecasting (81 frames), however, errors often accumulate late and can be underrepresented by short clips. We therefore also report FVMD-Long, computed on the full 81-frame future window as a single clip.

(ii) *FlowSmoothTV (FlowTV)* captures *spatial tearing*, where neighboring grid cells move inconsistently and produce large spatial flow gradients. We measure it as the total variation of per-frame flow on the grid, following TV-regularized optical flow [44]. Let $\hat{\mathbf{p}}_{t,i,j} \in \mathbb{R}^2$ be the predicted location at

Table 1: Comparison of trajectory generation with WHN (L). FVMD and flow diagnostics (FlowTV $\times 10^2$, DivCurlE $\times 10^3$; \downarrow) on Kinetics, RoboTAP, Kubric (MOVi-A; same config as WHN), and MagicData (E).

Metric	Method	Kinetics	RoboTAP	Kubric	MagicData (E)
FVMD \downarrow	WHN (L)	8999	7587	4872	10383
	Ours	3626	2467	1338	2968
FlowTV (10^2) \downarrow	WHN (L)	24.71	27.26	12.56	26.74
	Ours	7.53	6.03	6.03	7.11
DivCurlE (10^3) \downarrow	WHN (L)	34.69	37.39	9.89	40.04
	Ours	3.97	2.03	2.09	2.99

time t and define the flow $\mathbf{f}_{t,i,j} = (u_{t,i,j}, v_{t,i,j}) = \hat{\mathbf{p}}_{t,i,j} - \hat{\mathbf{p}}_{t-1,i,j}$ for $t \geq 1$. With grid spacing s (pixels), we use forward differences $\Delta_x u_{t,i,j} = (u_{t,i,j+1} - u_{t,i,j})/s$ and $\Delta_y u_{t,i,j} = (u_{t,i+1,j} - u_{t,i,j})/s$ (similarly for v), computed only at valid (visibility is true) neighbor pairs. For each time step, we define $\text{TV}_x(t) = \mathbb{E}_{i,j}^x [|\Delta_x u_{t,i,j}| + |\Delta_x v_{t,i,j}|]$ and $\text{TV}_y(t) = \mathbb{E}_{i,j}^y [|\Delta_y u_{t,i,j}| + |\Delta_y v_{t,i,j}|]$, where \mathbb{E}^x and \mathbb{E}^y average over valid horizontal and vertical pairs, respectively. We then average it over time:

$$\text{FlowTV} = \frac{1}{T-1} \sum_{t=1}^{T-1} (\text{TV}_x(t) + \text{TV}_y(t)). \quad (15)$$

Lower FlowTV means fewer spatial discontinuities.

(iii) *DivCurlEnergy (DivCurlE)*. DivCurlEnergy [6] captures *locally unstable deformation*, where predicted flow shows abrupt local expansion, contraction, or rotation. It measures large divergence (expansion/contraction) and curl (local rotation) in the predicted flow field. Using the same flow $\mathbf{f}_{t,i,j} = (u_{t,i,j}, v_{t,i,j})$, we form forward-difference divergence and curl on valid grid cells as $\text{div}(\mathbf{f}_t) = (\Delta_x u + \Delta_y v)/s$ and $\text{curl}(\mathbf{f}_t) = (\Delta_x v - \Delta_y u)/s$, and report their squared energy:

$$\text{DivCurlE} = \frac{1}{T-1} \sum_{t=1}^{T-1} \mathbb{E}_{i,j} [\text{div}(\mathbf{f}_t)_{i,j}^2 + \text{curl}(\mathbf{f}_t)_{i,j}^2], \quad (16)$$

where the expectation averages over valid cells (visibility-masked). Lower DivCurlE indicates less high-frequency spatial noise in the predicted motion.

(iv) *Visibility-masked Endpoint Error (VEPE)*. We evaluate TrajLoom-VAE reconstruction fidelity with endpoint error in pixel coordinates, averaged over visible points. Let $\mathbf{p}_{i,n} \in \mathbb{R}^2$ be the ground-truth location and $\hat{\mathbf{p}}_{i,n} \in \mathbb{R}^2$ the reconstructed location. The per-point error is $e_{i,n} = \|\hat{\mathbf{p}}_{i,n} - \mathbf{p}_{i,n}\|_2$, and we average over visible points using $v_{i,n} \in \{0, 1\}$:

$$\text{VEPE} = \frac{\sum_{i,n} v_{i,n} e_{i,n}}{\sum_{i,n} v_{i,n}}. \quad (17)$$

4.2 Quantitative Results.

Future-trajectory generation. Table 1 compares our generator and WHN (L) on real data (Kinetics, RoboTAP), synthetic data (Kubric), and MagicData (E). Kubric uses the same MOVi-A setup as WHN (L); we re-render the dataset for direct comparison. Our method consistently improves motion quality, reducing FVMD by 2.5–3.6 \times (e.g., 4872 to 1338 on Kubric). It also lowers FlowTV and DivCurlE, indicating fewer spatial discontinuities and more stable motion.

Track-VAE reconstruction. Table 2 reports trajectory VAE reconstruction fidelity. TrajLoom-VAE achieves low VEPE and outperforms WHN (L)-VAE by a large margin on all datasets. Performance remains stable as segment length increases from 24 to 81 frames, suggesting that the latent representation preserves long temporal windows without accumulating drift.

Table 2: Fidelity of trajectory VAE reconstruction. Visibility masked endpoint error (VEPE, (\downarrow)) for reconstructing 24 and 81 frame trajectory segments.

Frames	Method	Kinetics	RoboTAP	Kubric	MagicData (E)
24	WHN (L)-VAE	63.09	29.35	15.97	69.88
	Ours	1.99	1.59	0.75	1.72
81	WHN (L)-VAE	63.31	31.52	16.27	67.97
	Ours	2.04	1.61	0.77	1.72

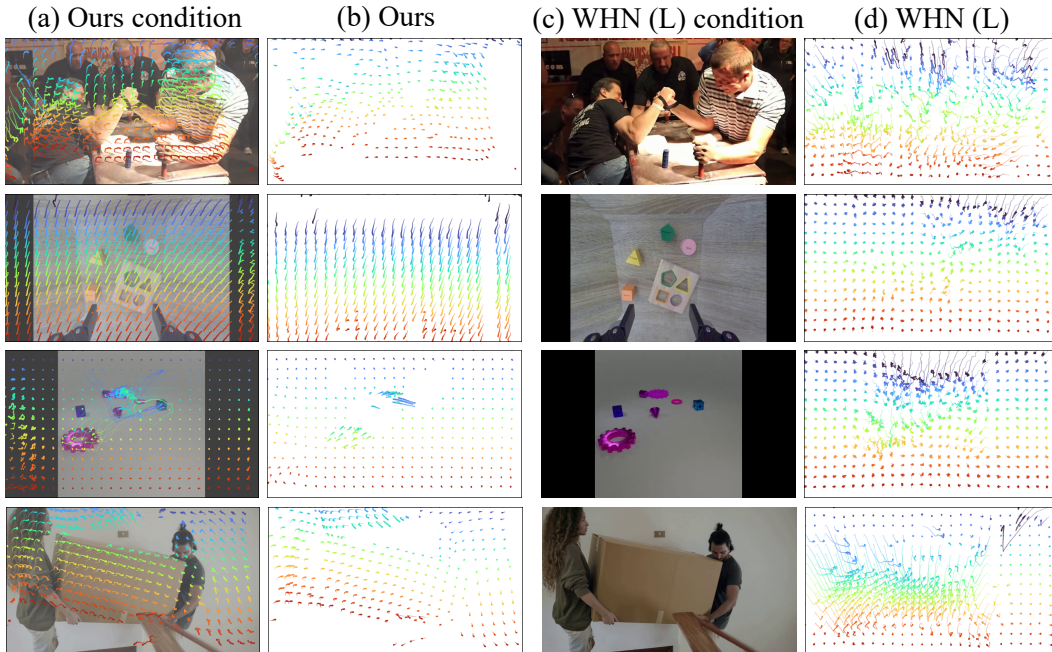


Figure 5: Comparison with WHN (L). Each row shows a dataset: Kinetics, RoboTAP, Kubric, and MagicData (E). Our method yields smoother and more coherent motion.

4.3 Qualitative Results

Figure 5 compares future trajectories across all benchmark sources. Conditioning on observed motion history produces futures that better continue current dynamics and remain spatially coherent, whereas WHN (L) more often shows drift and spatial tearing. More examples are provided in Appendix C.1.

4.4 Ablation Study

Table 3 shows the effect of Grid-Anchor Offset Encoding for 81-frame future generation. Removing offsets degrades long-horizon motion, increasing FVMD-Long and worsening FlowTV and DivCurlE, indicating more drift and tearing. We also ablate TrajLoom-VAE offset encoding and the spatiotemporal consistency regularizer, both of which improve reconstruction (Appendix D.1). Ablations of TrajLoom-Flow boundary hints are in Appendix D.3.

4.5 Downstream Applications

Predicted future trajectories can serve as motion-control signals for video generation with Wan-Move [5]. As shown in Figure 6, we use observed history trajectories to generate future trajectory fields with TrajLoom-Flow, then feed them to Wan-Move with a single input image to synthesize motion-consistent videos. This demonstrates that trajectory generation enables controllable motion continuation in downstream video generation.

Table 3: Ablation study with Grid-Anchor Offset Encoding on future 81 frames.

Metric	Method	Kinetics	RoboTAP	Kubric	MagicData (E)
FVMD-Long (10^{-3}) ↓	w/o offset	46.61	36.43	31.66	41.97
	Ours	35.06	21.75	7.24	28.27
FlowTV (10^2) ↓	w/o offset	15.92	15.26	15.54	15.01
	Ours	7.65	5.96	5.03	7.11
DivCurlE (10^3) ↓	w/o offset	19.10	16.27	17.66	16.13
	Ours	4.21	1.89	1.45	3.09



Figure 6: Trajectory-guided video generation with Wan-Move [5]. We use the observed history to generate a trajectory. Wan-Move then uses this trajectory, along with the condition image, to generate 81 frames, as shown in the third and fourth rows.

5 Conclusion

In this work, we present a framework for dense future-trajectory generation from observed history. Our approach combines Grid-Anchor Offset Encoding, a consistency-regularized TrajLoom-VAE, and the rectified-flow generator TrajLoom-Flow with explicit boundary cues and on-policy fine-tuning. Together, these components produce stable long-horizon motion and outperform state-of-the-art methods on TrajLoomBench in both quantitative and qualitative evaluations. For future work, we plan to improve trajectory controllability (e.g., user-driven trajectory editing) and further integrate our model with motion-guided generation and editing methods to improve versatility and accuracy.

Acknowledgements

This work was supported, in part, by the NSERC DG Grant (No. RGPIN-2022-04636), the NSERC Alliance Grant (ALLRP 604621-25), the Vector Institute for AI, and the Canada CIFAR AI Chair program. Resources used in preparing this research were provided, in part, by the Province of Ontario, the Government of Canada through the Digital Research Alliance of Canada alliance.can.ca, and companies sponsoring the Vector Institute www.vectorinstitute.ai/#partners, and Advanced Research Computing at the University of British Columbia. Additional resource was provided by the Canada Foundation for Innovation (CFI) via the John R. Evans Leaders Fund (JELF).

References

- [1] Homanga Bharadhwaj, Roozbeh Mottaghi, Abhinav Gupta, and Shubham Tulsiani. Track2act: Predicting point tracks from internet videos enables generalizable robot manipulation. In *European Conference on Computer Vision*, pages 306–324. Springer, 2024.
- [2] Gabrijel Boduljak, Laurynas Karazija, Iro Laina, Christian Rupprecht, and Andrea Vedaldi. What happens next? anticipating future motion by generating point trajectories. In *The Fourteenth International Conference on Learning Representations*, 2026. URL <https://openreview.net/forum?id=t1vMY11yhe>.
- [3] Ryan Burgert, Yuancheng Xu, Wenqi Xian, Oliver Pilarski, Pascal Clausen, Mingming He, Li Ma, Yitong Deng, Lingxiao Li, Mohsen Mousavi, et al. Go-with-the-flow: Motion-controllable video diffusion models using real-time warped noise. In *Proceedings of the Computer Vision and Pattern Recognition Conference*, pages 13–23, 2025.
- [4] Ricky TQ Chen, Yulia Rubanova, Jesse Bettencourt, and David K Duvenaud. Neural ordinary differential equations. *Advances in neural information processing systems*, 31, 2018.
- [5] Ruihang Chu, Yefei He, Zhekai Chen, Shiwei Zhang, Xiaogang Xu, Bin Xia, Dingdong WANG, Hongwei Yi, Xihui Liu, Hengshuang Zhao, Yu Liu, Yingya Zhang, and Yujiu Yang. Wan-move: Motion-controllable video generation via latent trajectory guidance. In *The Thirty-ninth Annual Conference on Neural Information Processing Systems*, 2025. URL <https://openreview.net/forum?id=1HW93LKaUk>.
- [6] Thomas Corpetti, Dominique Heitz, Georges Arroyo, Etienne M emin, and Alina Santa-Cruz. Fluid experimental flow estimation based on an optical-flow scheme. *Experiments in fluids*, 40(1):80–97, 2006.
- [7] Yufan Deng, Ruida Wang, Yuhao Zhang, Yu-Wing Tai, and Chi-Keung Tang. Dragvideo: Interactive drag-style video editing. In *European conference on computer vision*, pages 183–199. Springer, 2024.
- [8] Carl Doersch, Ankush Gupta, Larisa Markeeva, Adria Recasens, Lucas Smaira, Yusuf Aytar, Joao Carreira, Andrew Zisserman, and Yi Yang. Tap-vid: A benchmark for tracking any point in a video. *Advances in Neural Information Processing Systems*, 35:13610–13626, 2022.
- [9] Carl Doersch, Yi Yang, Mel Vecerik, Dilara Gokay, Ankush Gupta, Yusuf Aytar, Joao Carreira, and Andrew Zisserman. Tapir: Tracking any point with per-frame initialization and temporal refinement. In *Proceedings of the IEEE/CVF International Conference on Computer Vision*, pages 10061–10072, 2023.
- [10] Carl Doersch, Pauline Luc, Yi Yang, Dilara Gokay, Skanda Koppula, Ankush Gupta, Joseph Heyward, Ignacio Rocco, Ross Goroshin, Joao Carreira, et al. Bootstap: Bootstrapped training for tracking-any-point. In *Proceedings of the Asian Conference on Computer Vision*, pages 3257–3274, 2024.
- [11] John R Dormand and Peter J Prince. A family of embedded runge-kutta formulae. *Journal of computational and applied mathematics*, 6(1):19–26, 1980.
- [12] Daniel Geng, Charles Herrmann, Junhwa Hur, Forrester Cole, Serena Zhang, Tobias Pfaff, Tatiana Lopez-Guevara, Yusuf Aytar, Michael Rubinstein, Chen Sun, et al. Motion prompting: Controlling video generation with motion trajectories. In *Proceedings of the Computer Vision and Pattern Recognition Conference*, pages 1–12, 2025.
- [13] Klaus Greff, Francois Belletti, Lucas Beyer, Carl Doersch, Yilun Du, Daniel Duckworth, David J Fleet, Dan Gnanapragasam, Florian Golemo, Charles Herrmann, et al. Kubric: A scalable dataset generator. In *Proceedings of the IEEE/CVF conference on computer vision and pattern recognition*, pages 3749–3761, 2022.
- [14] Adam W Harley, Zhaoyuan Fang, and Katerina Fragkiadaki. Particle video revisited: Tracking through occlusions using point trajectories. In *European Conference on Computer Vision*, pages 59–75. Springer, 2022.

- [15] Adam W. Harley, Yang You, Xinglong Sun, Yang Zheng, Nikhil Raghuraman, Yunqi Gu, Sheldon Liang, Wen-Hsuan Chu, Achal Dave, Pavel Tokmakov, Suya You, Rares Ambrus, Katerina Fragkiadaki, and Leonidas J. Guibas. AllTracker: Efficient dense point tracking at high resolution. In *ICCV*, 2025.
- [16] Peter J Huber. Robust estimation of a location parameter. In *Breakthroughs in statistics: Methodology and distribution*, pages 492–518. Springer, 1992.
- [17] Nikita Karaev, Yuri Makarov, Jianyuan Wang, Natalia Neverova, Andrea Vedaldi, and Christian Rupprecht. Cotracker3: Simpler and better point tracking by pseudo-labelling real videos. In *Proceedings of the IEEE/CVF International Conference on Computer Vision*, pages 6013–6022, 2025.
- [18] Will Kay, João Carreira, Karen Simonyan, Brian Zhang, Chloe Hillier, Sudheendra Vijayanarasimhan, Fabio Viola, Tim Green, Trevor Back, Paul Natsev, Mustafa Suleyman, and Andrew Zisserman. The kinetics human action video dataset. *CoRR*, abs/1705.06950, 2017. URL <http://arxiv.org/abs/1705.06950>.
- [19] Diederik P. Kingma and Jimmy Ba. Adam: A method for stochastic optimization. In Yoshua Bengio and Yann LeCun, editors, *3rd International Conference on Learning Representations, ICLR 2015, San Diego, CA, USA, May 7-9, 2015, Conference Track Proceedings*, 2015. URL <http://arxiv.org/abs/1412.6980>.
- [20] Diederik P. Kingma and Max Welling. Auto-encoding variational bayes. *CoRR*, abs/1312.6114, 2013.
- [21] Quanhao Li, Zhen Xing, Rui Wang, Hui Zhang, Qi Dai, and Zuxuan Wu. Magicmotion: Controllable video generation with dense-to-sparse trajectory guidance. In *Proceedings of the IEEE/CVF International Conference on Computer Vision (ICCV)*, pages 12112–12123, October 2025.
- [22] Yaron Lipman, Ricky TQ Chen, Heli Ben-Hamu, Maximilian Nickel, and Matthew Le. Flow matching for generative modeling. In *The Eleventh International Conference on Learning Representations*, 2023.
- [23] Jiahe Liu, Youran Qu, Qi Yan, Xiaohui Zeng, Lele Wang, and Renjie Liao. Fréchet video motion distance: A metric for evaluating motion consistency in videos. *arXiv preprint arXiv:2407.16124*, 2024.
- [24] Xingchao Liu, Chengyue Gong, and qiang liu. Flow straight and fast: Learning to generate and transfer data with rectified flow. In *The Eleventh International Conference on Learning Representations*, 2023. URL <https://openreview.net/forum?id=XVjTT1nw5z>.
- [25] Ilya Loshchilov and Frank Hutter. Decoupled weight decay regularization. In *International Conference on Learning Representations*, 2019. URL <https://openreview.net/forum?id=Bkg6RiCqY7>.
- [26] Xin Ma, Yaohui Wang, Xinyuan Chen, Gengyun Jia, Ziwei Liu, Yuan-Fang Li, Cunjian Chen, and Yu Qiao. Latte: Latent diffusion transformer for video generation. *Transactions on Machine Learning Research*, 2025.
- [27] Koichi Namekata, Sherwin Bahmani, Ziyi Wu, Yash Kant, Igor Gilitschenski, and David B. Lindell. SG-i2v: Self-guided trajectory control in image-to-video generation. In *The Thirteenth International Conference on Learning Representations*, 2025. URL <https://openreview.net/forum?id=uQjySppU9x>.
- [28] Xingang Pan, Ayush Tewari, Thomas Leimkühler, Lingjie Liu, Abhimitra Meka, and Christian Theobalt. Drag your gan: Interactive point-based manipulation on the generative image manifold. In *ACM SIGGRAPH 2023 conference proceedings*, pages 1–11, 2023.
- [29] William Peebles and Saining Xie. Scalable diffusion models with transformers. In *Proceedings of the IEEE/CVF international conference on computer vision*, pages 4195–4205, 2023.

- [30] Adam Polyak, Amit Zohar, Andrew Brown, Andros Tjandra, Animesh Sinha, Ann Lee, Apoorv Vyas, Bowen Shi, Chih-Yao Ma, Ching-Yao Chuang, et al. Movie gen: A cast of media foundation models. *arXiv preprint arXiv:2410.13720*, 2024.
- [31] Colin Raffel, Noam Shazeer, Adam Roberts, Katherine Lee, Sharan Narang, Michael Matena, Yanqi Zhou, Wei Li, and Peter J. Liu. Exploring the limits of transfer learning with a unified text-to-text transformer. *Journal of Machine Learning Research*, 21(140):1–67, 2020. URL <http://jmlr.org/papers/v21/20-074.html>.
- [32] Yujun Shi, Chuhui Xue, Jun Hao Liew, Jiachun Pan, Hanshu Yan, Wenqing Zhang, Vincent YF Tan, and Song Bai. Dragdiffusion: Harnessing diffusion models for interactive point-based image editing. In *Proceedings of the IEEE/CVF conference on computer vision and pattern recognition*, pages 8839–8849, 2024.
- [33] Karen Simonyan and Andrew Zisserman. Two-stream convolutional networks for action recognition in videos. *Advances in neural information processing systems*, 27, 2014.
- [34] Alexander Tong, Kilian FATRAS, Nikolay Malkin, Guillaume Huguet, Yanlei Zhang, Jarrid Rector-Brooks, Guy Wolf, and Yoshua Bengio. Improving and generalizing flow-based generative models with minibatch optimal transport. *Transactions on Machine Learning Research*, 2024. ISSN 2835-8856. URL <https://openreview.net/forum?id=CD9Snc73AW>. Expert Certification.
- [35] Mel Vecerik, Carl Doersch, Yi Yang, Todor Davchev, Yusuf Aytar, Guangyao Zhou, Raia Hadsell, Lourdes Agapito, and Jon Scholz. Robotap: Tracking arbitrary points for few-shot visual imitation. In *2024 IEEE International Conference on Robotics and Automation (ICRA)*, pages 5397–5403. IEEE, 2024.
- [36] Jacob Walker, Carl Doersch, Abhinav Gupta, and Martial Hebert. An uncertain future: Forecasting from static images using variational autoencoders. In *European conference on computer vision*, pages 835–851. Springer, 2016.
- [37] Team Wan, Ang Wang, Baole Ai, Bin Wen, Chaojie Mao, Chen-Wei Xie, Di Chen, Feiwu Yu, Haiming Zhao, Jianxiao Yang, et al. Wan: Open and advanced large-scale video generative models. *arXiv preprint arXiv:2503.20314*, 2025.
- [38] Qianqian Wang, Yen-Yu Chang, Ruojin Cai, Zhengqi Li, Bharath Hariharan, Aleksander Holynski, and Noah Snavely. Tracking everything everywhere all at once. In *Proceedings of the IEEE/CVF International Conference on Computer Vision*, pages 19795–19806, 2023.
- [39] Xiang Wang, Hangjie Yuan, Shiwei Zhang, Dayou Chen, Jiuniu Wang, Yingya Zhang, Yujun Shen, Deli Zhao, and Jingren Zhou. Videocomposer: Compositional video synthesis with motion controllability. *Advances in Neural Information Processing Systems*, 36:7594–7611, 2023.
- [40] Zhouxia Wang, Ziyang Yuan, Xintao Wang, Yaowei Li, Tianshui Chen, Menghan Xia, Ping Luo, and Ying Shan. Motionctrl: A unified and flexible motion controller for video generation. In *ACM SIGGRAPH 2024 Conference Papers*, pages 1–11, 2024.
- [41] Chuan Wen, Xingyu Lin, John So, Kai Chen, Qi Dou, Yang Gao, and Pieter Abbeel. Any-point trajectory modeling for policy learning, 2023.
- [42] Jiange Yang, Haoyi Zhu, Yating Wang, Gangshan Wu, Tong He, and Limin Wang. Tra-moe: Learning trajectory prediction model from multiple domains for adaptive policy conditioning. In *Proceedings of the IEEE/CVF Conference on Computer Vision and Pattern Recognition*, pages 6960–6970, 2025.
- [43] Shengming Yin, Chenfei Wu, Jian Liang, Jie Shi, Houqiang Li, Gong Ming, and Nan Duan. Dragnuwa: Fine-grained control in video generation by integrating text, image, and trajectory. *arXiv preprint arXiv:2308.08089*, 2023.
- [44] Christopher Zach, Thomas Pock, and Horst Bischof. A duality based approach for realtime tv-l 1 optical flow. In *Joint pattern recognition symposium*, pages 214–223. Springer, 2007.

- [45] Zewei Zhang, Huan Liu, Jun Chen, and Xiangyu Xu. Gooddrag: Towards good practices for drag editing with diffusion models. In *The Thirteenth International Conference on Learning Representations*, 2025.
- [46] Zhenghao Zhang, Junchao Liao, Menghao Li, Zuozhuo Dai, Bingxue Qiu, Siyu Zhu, Long Qin, and Weizhi Wang. Tora: Trajectory-oriented diffusion transformer for video generation. In *Proceedings of the Computer Vision and Pattern Recognition Conference*, pages 2063–2073, 2025.
- [47] Yang Zheng, Adam W Harley, Bokui Shen, Gordon Wetzstein, and Leonidas J Guibas. Pointodyssey: A large-scale synthetic dataset for long-term point tracking. In *Proceedings of the IEEE/CVF International Conference on Computer Vision*, pages 19855–19865, 2023.

A Model and Training Details

Backbone. Following WHN [2], both TrajLoom-VAE and TrajLoom-Flow use a DiT-style transformer [29] with the Latte design [26]. We operate on trajectory fields at 480×832 with patch size 32, yielding $15 \times 26 = 390$ spatial tokens per frame.

A.1 TrajLoom-VAE

Architecture. TrajLoom-VAE encodes 81-frame trajectory segments (2D offsets; Section 3.1) into a compact spatiotemporal latent tensor with $C=16$ channels. We use a Latte encoder/decoder with 16 blocks each, 8 attention heads, and hidden size 512. A temporal convolutional compression module with stride 4 reduces the temporal length from 81 to 21 latent steps.

Objective. We train TrajLoom-VAE with a visibility-masked Huber reconstruction loss, a KL penalty with $\beta = 5 \times 10^{-5}$, and the spatiotemporal consistency regularizer from Section 3.2. The regularizer weights are $\lambda_{\text{temporal}} = 0.1$ and $\lambda_{\text{spatial}} = 0.2$. For the multiscale spatial term, we use $\mathcal{S} = \{1, 2, 4\}$ and $\alpha_\delta = 1/\delta$, i.e. $\{1, 0.5, 0.25\}$ for hop distances $\{1, 2, 4\}$.

Optimization. We optimize with AdamW [19, 25] using a learning rate of 2×10^{-5} , $(\beta_1, \beta_2) = (0.9, 0.999)$, weight decay of 0, batch size 4, and gradient accumulation 2 on 2 RTX PRO 6000 (effective batch size 16), using bf16 mixed precision and clipping gradients to keep the norm at 1.0, training for a total of 30k steps.

A.2 TrajLoom-Flow

Architecture and conditioning. TrajLoom-Flow predicts future TrajLoom-VAE latents with a Latte [26] generator of 16 blocks, 12 heads, and hidden size 768 (matching WHN (L) scale). In our setting, \mathbf{c} includes history trajectory latents \mathbf{z}^p , tokenized history visibility, history-video features, and a pooled text embedding [31].

Latent normalization. Before training TrajLoom-Flow, we compute per-channel mean and std statistics of TrajLoom-VAE latents on the training set and apply channel-wise normalization. The generator is trained in the normalized latent space; decoding uses the inverse transform.

Flow-matching pretraining. We train with rectified flow matching in latent space (Section 3.3.2) using tube noise $\sigma = 0.05$. We sample flow time $t \in (0, 1)$ from a mixture: with probability 0.2, $t \sim \text{Uniform}(0, 0.1)$; otherwise $t = \sigma(\mathcal{N}(0, 1))$ (clamped to $[10^{-5}, 1 - 10^{-5}]$) [30, 2]. We supervise with a token-masked MSE using future visibility pooled to the latent grid, and we assign a small weight 0.01 to invisible tokens so they are not completely ignored.

Source distribution (z_0). We use the boundary hints: z_0 is sampled as Gaussian noise, and the first future latent slice is anchored to the last history latent slice (with additive noise of std 0.1) to encourage continuity at the history–future boundary (Section 3.3.1).

Optimization. We optimize with AdamW (weight decay 0) at a learning rate of 6×10^{-5} , batch size 32 on 4 H100 with an effective batch size of 128, bf16 mixed precision, and gradient clipping at 1.0. We enable checkpointing for activation to reduce memory usage. And we trained 100k steps in total.

A.3 On-policy K -step fine-tuning

To reduce the train–test mismatch from ODE sampling (Section 3.3.3), we fine-tune TrajLoom-Flow with the on-policy K -step rollout objective. We use $K=8$ Euler rollout steps on a logit-spaced time grid in $[t_\epsilon, 1 - t_\epsilon]$ with $t_\epsilon = 10^{-5}$, and clamp denominators with $t_\epsilon = 10^{-3}$. The rollout loss uses weights $w_1 = 1.0$ (toward \mathbf{z}_1), $w_0 = 0.5$ (toward \mathbf{z}_0), and endpoint-consistency weight γ as 0.1. For stability, the endpoint-consistency term is computed *without* visibility masking (i.e., over all tokens). We apply the rollout loss on a small sub-batch of 8 samples per iteration, with overall weight $\lambda_{k\text{-step}} = 0.1$. And fine-tune using learning rate 1×10^{-5} while keeping other settings unchanged.

B Further Analyses of Offset Encoding and Consistency Regularization

This section provides further analyses of two key design choices in our method. We first quantify how Grid-Anchor Offset Encoding reduce location-dependent bias, and then illustrate why pointwise reconstruction alone is insufficient without spatiotemporal consistency regularization.

B.1 Quantifying Location Bias Removed by Grid-Anchored Offsets

This appendix provides details for the model-free analysis in Figure 3b. The goal is to measure how much of the coordinate variance is explained purely by the *grid location* (a static spatial baseline), compared to the remaining variance that comes from *temporal motion*.

We use dense point tracks extracted by AllTracker [15] on a stride- s grid (here $s = 32$) at resolution $H \times W = 480 \times 832$. Each track corresponds to a fixed grid cell $n \in \{1, \dots, N\}$, and provides per-frame 2D coordinates and visibility. We convert pixel coordinates to normalized coordinates in $[-1, 1]$ and form offsets by subtracting the (normalized) center anchor of the corresponding stride cell, i.e. $\mathbf{X}_{n,t} = \mathbf{D}_{n,t} - \mathbf{G}_n$. We evaluate on 128 randomly sampled clips.

For a single coordinate axis d (either D_x , D_y , X_x , or X_y), let $d_{n,t}$ be the value at grid location n and time t , with visibility $v_{n,t} \in \{0, 1\}$. For each location n , we compute a visibility-weighted time average $\mu_n = \frac{\sum_t v_{n,t} d_{n,t}}{\sum_t v_{n,t}}$ as the *location baseline*, and a visibility-weighted temporal variance around that baseline $\sigma_n^2 = \frac{\sum_t v_{n,t} (d_{n,t} - \mu_n)^2}{\sum_t v_{n,t}}$.

We then decompose the total coordinate variance into a between-location term and a within-location term. Let $\text{Var}_n(\cdot)$ and $\mathbb{E}_n[\cdot]$ denote variance and mean over grid locations n . We define the fraction of variance explained by grid location as:

$$\text{Var}(d) = \text{Var}_n(\mu_n) + \mathbb{E}_n[\sigma_n^2], \quad \text{Explained}(\%) = 100 \cdot \frac{\text{Var}_n(\mu_n)}{\text{Var}_n(\mu_n) + \mathbb{E}_n[\sigma_n^2]}. \quad (18)$$

Here, $\text{Var}(d)$ denotes the total variance under this decomposition: $\text{Var}_n(\mu_n)$ measures how much coordinates differ across grid locations due to the static spatial baseline, while $\mathbb{E}_n[\sigma_n^2]$ measures the average temporal variance (motion) at a fixed location. A high explained percentage indicates that most coordinate variation is attributable to grid position rather than motion. As shown in Figure 3b, absolute coordinates have high explained variance, while offsets strongly reduce this location-driven component.

B.2 Why spatiotemporal consistency regularization is needed

In this section, we explain why pointwise reconstruction loss alone is insufficient and motivate the need for spatiotemporal consistency regularization. Pointwise reconstruction alone does not uniquely determine a physically plausible motion trajectory. To illustrate this, we consider a 1D trajectory with full visibility and ground truth $x(t) = t$ for discrete time t . We compare two reconstructions that have the same per-frame deviation magnitude: a *smooth* reconstruction with a constant bias, $\hat{x}_{\text{smooth}}(t) = t + b$, and a *jittery* reconstruction with an alternating bias, $\hat{x}_{\text{jitter}}(t) = t + b(-1)^t$. Both reconstructions have identical pointwise error $|\hat{x}(t) - x(t)| = |b|$ at every frame, and therefore can achieve the same masked Huber reconstruction loss L_{rec} (for any Huber threshold that treats these deviations similarly).

However, the two reconstructions imply very different *motion*. The ground-truth velocity is constant, $\Delta x(t) = x(t) - x(t-1) = 1$. The smooth reconstruction preserves this, $\Delta \hat{x}_{\text{smooth}}(t) = 1$, while the jittery reconstruction alternates its frame-to-frame displacement, $\Delta \hat{x}_{\text{jitter}}(t) = 1 + 2b(-1)^t$. As a result, the velocity-matching term penalizes the jittery solution even though L_{rec} cannot distinguish it. The same issue generalizes to dense 2D trajectory fields: reconstructions can match per-frame positions yet exhibit temporal jitter and locally inconsistent motion across neighboring points. Our spatiotemporal consistency regularizer directly targets these failure modes by matching temporal displacements (L_{temporal}) and neighbor relations (L_{spatial}), as shown in Figure 7.

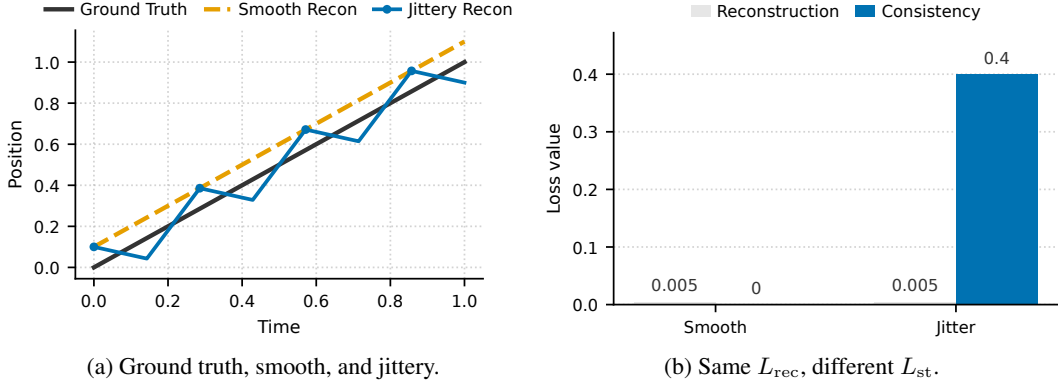


Figure 7: 1D toy example: pointwise reconstruction loss does not guarantee realistic motion. Both smooth and jittery reconstructions of $x(t) = t$ can match L_{rec} , but only the smooth one aligns with ground truth motion. Consistency regularization separates realistic from unrealistic solutions.

C Additional Qualitative Results

C.1 More Comparisons with WHN

Figure 8 shows additional side-by-side comparisons with WHN (L). Each row is a different clip; (a)(b) show our history condition and predicted future, while (c)(d) show WHN (L) with its image condition and predicted future. Our results more consistently preserve long-horizon coherence with fewer drift/tearing artifacts.

C.2 More Downstream Examples

We further demonstrate downstream controllable video synthesis using Wan-Move [5]. Given the observed history, we first sample 81-frame future trajectories with TrajLoom-Flow. We then provide Wan-Move with the predicted trajectories and the conditioning image to generate an 81-frame video that follows the generated motion. Figure 9 shows additional examples.

D Additional Quantitative Studies

This section presents additional empirical results beyond the main paper. We first report ablations and training dynamics for TrajLoom-VAE, and then provide component ablations and sampling analyses for TrajLoom-Flow.

D.1 TrajLoom-VAE Ablations

We ablate two components of TrajLoom-VAE: (i) the Grid-Anchor Offset Encoding and (ii) the spatiotemporal consistency regularizer. Table 4 reports VEPE (pixels; lower is better) for reconstructing 24- and 81-frame trajectory segments. Removing offset encoding consistently increases reconstruction error across datasets and horizons, confirming that offsets reduce location-dependent bias and simplify trajectory modeling. Removing the consistency regularizer also degrades VEPE, especially on longer windows, consistent with the regularizer suppressing temporal jitter and improving local coherence in the reconstructed motion.

D.2 VAE Training Dynamics

Figure 10 plots the TrajLoom-VAE masked L_1 reconstruction loss for our full model and two ablations. Removing the Grid-Anchor Offset Encoding leads to worse convergence and a gradually increasing loss, consistent with overfitting to location-dependent coordinate biases in absolute space. In contrast, removing the spatiotemporal consistency regularizer yields a higher-loss plateau, indicating underfitting: pointwise reconstruction alone does not sufficiently constrain motion structure.

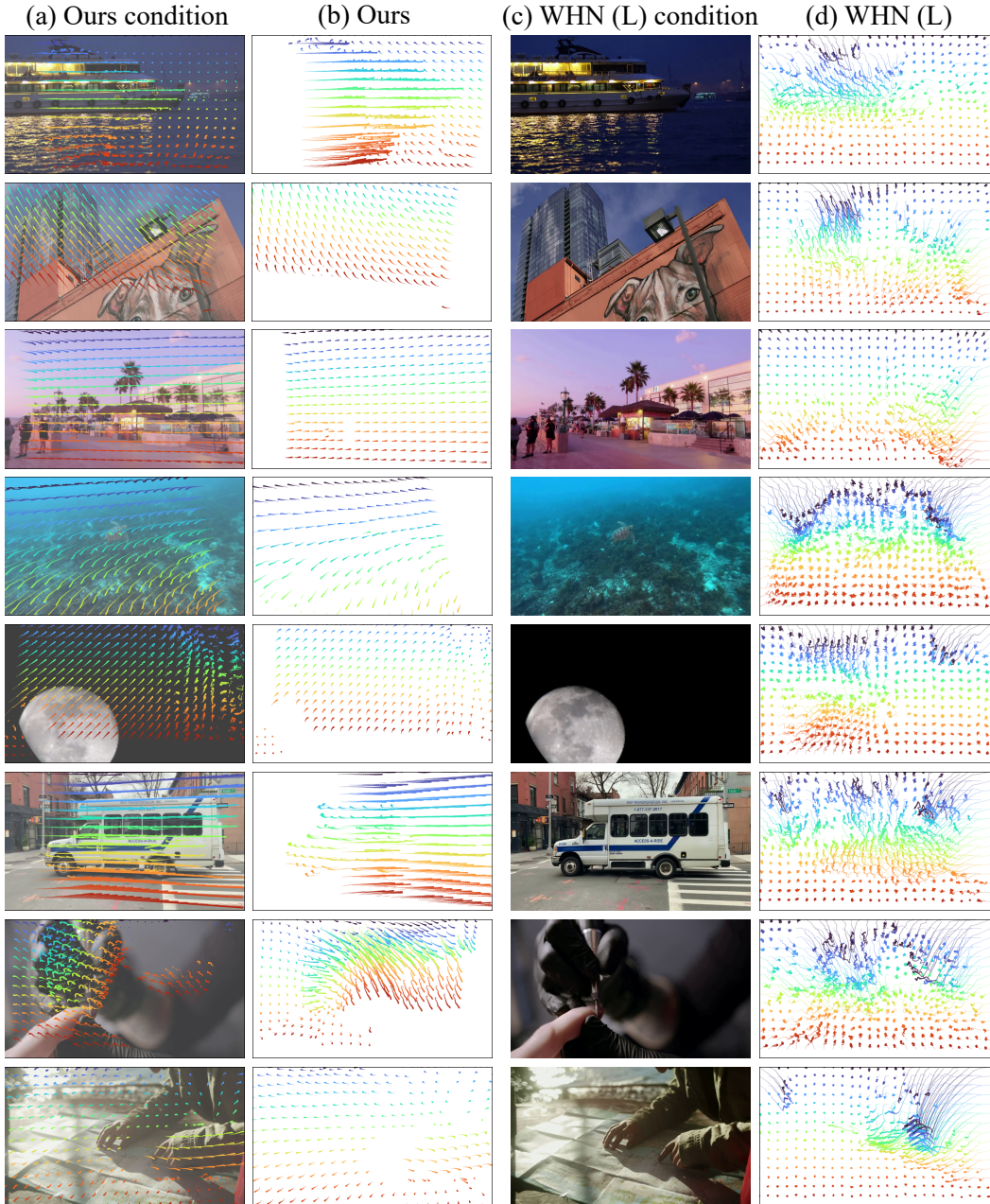


Figure 8: More Comparison with WHN (L).

Together, these trends support our design: offset encoding makes the learning problem better conditioned by removing global-position bias, while the regularizer provides motion-level constraints that help the latent space capture temporally smooth and locally coherent trajectories.

D.3 TrajLoom-Flow Ablation Study

This appendix provides additional ablations on TrajLoom-Flow components described in Section 3.3.1, including boundary hints and on-policy fine-tuning. All results are computed on 81-frame future prediction using Euler integration with 10 steps, and report the same motion and flow-field diagnostics as in the main paper.

We ablate:

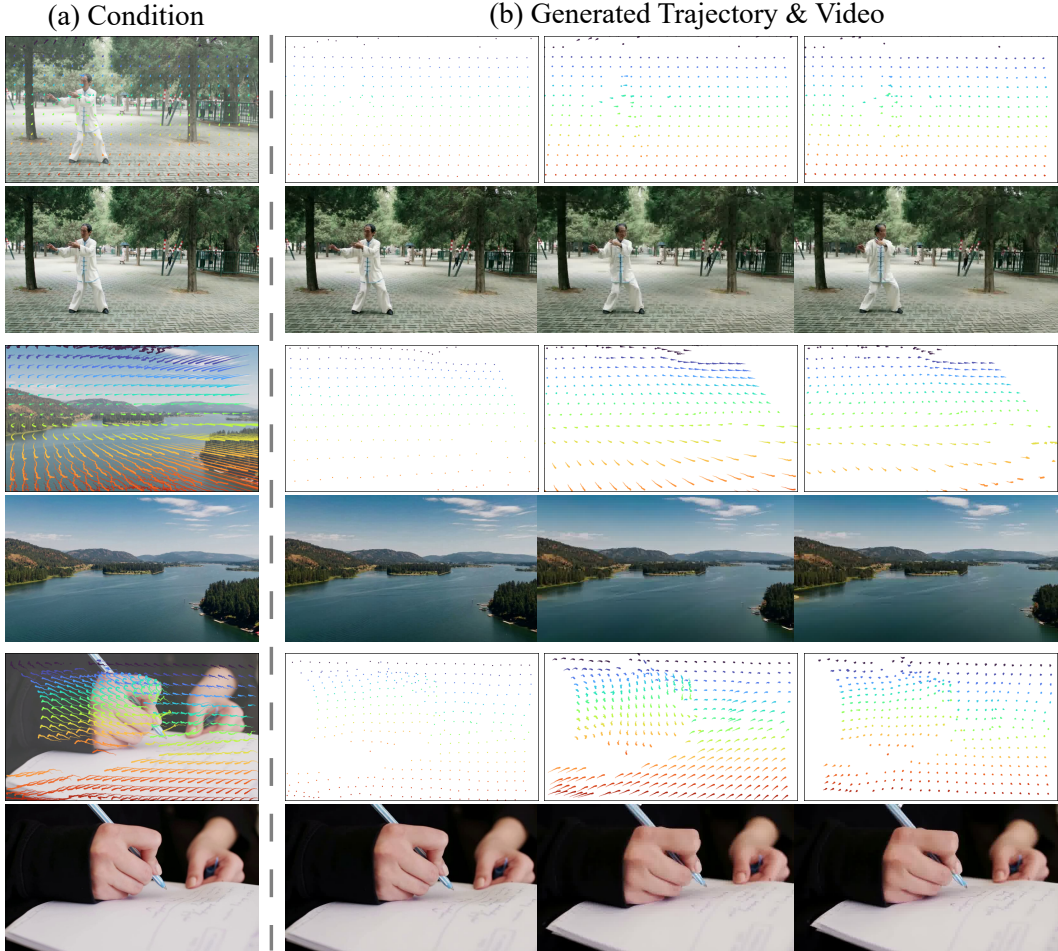


Figure 9: Additional Wan-Move results driven by our predicted trajectories. Left: conditioning inputs (history trajectory and the conditioning image). Right: our generated 81-frame future trajectories and the corresponding 81-frame videos synthesized by Wan-Move.

Table 4: TrajLoom-VAE ablations. Effect of Grid-Anchor Offset Encoding and spatiotemporal consistency regularization on VEPE (\downarrow).

Frames	Method	Kinetics	RoboTAP	Kubic	MagicData (E)
24	w/o offset	4.24	3.98	3.26	3.91
	w/o regularizer	2.99	2.35	1.42	2.65
	Ours	1.99	1.59	0.75	1.72
81	w/o offset	4.30	4.01	3.24	3.99
	w/o regularizer	3.11	2.41	1.47	3.99
	Ours	2.04	1.61	0.77	1.72

1. **History fusion:** removing the token-aligned history fusion module, so history is provided only through the conditioning stream c .
2. **Boundary anchoring:** disabling first-slice boundary anchoring, i.e. not adding $z(-1, n)$ to $z_0(0, n)$.
3. **On-policy fine-tuning:** training with flow matching only (Section 3.3.2), i.e. setting $\lambda_{k\text{-step}} = 0$ and omitting the on-policy K -step fine-tuning stage.

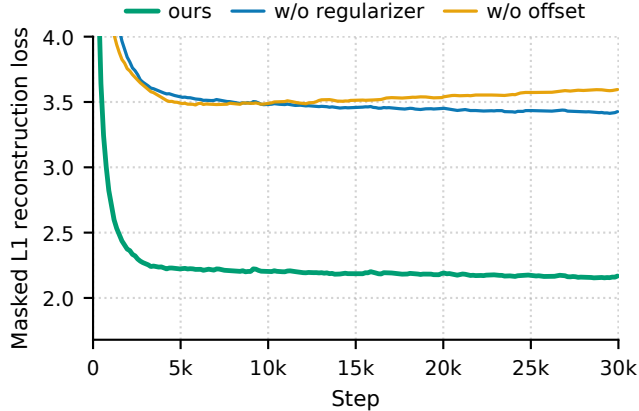


Figure 10: TrajLoom-VAE training curves. Masked L_1 reconstruction metric vs. training step. Using Grid-Anchor Offset Encoding and the spatiotemporal regularizer yields faster, more stable convergence and a substantially lower loss than removing offsets or the regularizer.

Table 5: Ablation study with flow-field diagnostics (generator components). Metrics are computed on 81-frame future prediction. Lower is better (\downarrow). All results use Euler integration with 10 steps. **w/o fusion** removes the token-aligned history fusion module; **w/o anchoring** disables boundary anchoring of the first future latent slice ; **20k steps** is an early flow-matching checkpoint of the generator; **w/o on-policy** matches the full flow-matching training budget of our method but omits the on-policy K -step fine-tuning stage.

Metric	Setting	Kinetics	RoboTAP	Kubric	MagicData (E)
FVMD-Long (10^{-3}) \downarrow	w/o fusion	39.60	28.86	16.38	33.87
	w/o anchoring	43.50	33.12	20.29	37.11
	20 k steps	40.13	28.81	17.02	33.51
	w/o on-policy	38.87	27.38	13.86	31.71
	Ours	35.06	21.75	7.24	28.27
FlowTV (10^2) \downarrow	w/o fusion	9.66	8.66	9.56	8.50
	w/o anchoring	10.07	9.11	9.80	8.90
	20 k steps	9.99	9.09	9.99	8.94
	w/o on-policy	8.98	8.22	8.90	8.16
	Ours	7.65	5.96	5.03	7.11
DivCurlE (10^3) \downarrow	w/o fusion	7.29	5.49	11.24	5.04
	w/o anchoring	7.83	5.85	11.71	5.53
	20 k steps	8.09	5.79	11.44	5.63
	w/o on-policy	6.11	4.58	8.12	4.41
	Ours	4.21	1.89	1.45	3.09

In addition, Table 5 reports an early flow-matching checkpoint (20k steps) and a full-budget model trained without on-policy fine-tuning (w/o on-policy) to separate the effect of training duration from the proposed on-policy stage. Overall, longer flow-matching training improves motion quality, but on-policy fine-tuning consistently provides further gains across datasets. Among the boundary-hint variants, disabling first-slice boundary anchoring (w/o anchoring) causes the largest degradation, while removing token-aligned history fusion (w/o fusion) yields a smaller but consistent drop.

D.4 Advanced ODE Solver and More Sampling Steps

Our generator is sampled by integrating the rectified-flow ODE in the latent space. In the main paper, we use a lightweight Euler solver with 10 steps as the default for efficiency, to match the WHN setting [2]. Here we study the effect of using a higher-order sampler with more function

Table 6: Effect of sampler choice and step count. Metrics are computed on 81-frame future prediction; lower is better (\downarrow). Entries marked with * use Dormand–Prince (DOPRI5) with 100 steps, while unmarked entries use Euler with 10 steps (default).

Metric	Method	Kinetics	RoboTAP	Kubric	MagicData (E)
FVMD \downarrow	WHN (L)	8999	7587	4872	10383
	WHN (L)*	8755	5855	6284	9691
	Ours	3626	2467	1338	2968
	Ours*	3182	2546	1724	2358
FlowTV (10^2) \downarrow	WHN (L)	24.71	27.26	12.56	26.74
	WHN (L)*	22.06	14.46	18.41	14.46
	Ours	7.53	6.03	6.03	7.11
	Ours*	4.50	3.40	3.09	3.72
DivCurlE (10^3) \downarrow	WHN (L)	34.69	37.39	9.89	40.04
	WHN (L)*	28.52	14.41	17.58	14.41
	Ours	3.97	2.03	2.09	2.99
	Ours*	2.86	1.17	1.10	1.59

evaluations: we additionally evaluate both WHN (L) [2] and our method using the Dormand–Prince solver (DOPRI5) [11] with 100 steps, following common practice for improving ODE sampling quality [34]. We denote results obtained with DOPRI5-100 by a superscript *, indicating the use of this solver. Entries without * use the default Euler-10 setting.

Table 6 shows that increasing solver accuracy can improve sampling quality, especially in the flow-field diagnostics: for our method, DOPRI5-100 consistently reduces FlowTV and DivCurlE across datasets, indicating smoother and more locally coherent predicted motion.

Importantly, our method substantially outperforms WHN (L) under both solver settings, indicating that the gains are not dependent on a particular sampler; we use Euler-10 as a strong efficiency-quality trade-off, and DOPRI5-100 as an optional higher-cost setting when additional smoothness is desired.

E Conditioning and Auxiliary Components

This section describes additional conditioning and auxiliary components used in the full pipeline. We first detail the boundary hints used by TrajLoom-Flow, then summarize the camera-motion caption augmentation used to enrich text conditioning, and finally describe the visibility predictor.

E.1 Boundary Hints Details

This appendix specifies the two *boundary hints* used by TrajLoom-Flow (Section 3.3.1): (i) a boundary-anchored source state \mathbf{z}_0 for rectified-flow sampling, and (ii) a token-aligned fusion term that injects boundary information from \mathbf{z}^p into the model input.

Boundary-anchored source state \mathbf{z}_0 . Let $\mathbf{z}(-1, n)$ denote the last history latent slice. We initialize the source state by repeating this boundary latent across future latent time indices k and adding Gaussian noise:

$$\mathbf{z}_0(k, n) = \mathbf{z}(-1, n) + \sigma_0 \boldsymbol{\eta}(k, n), \quad \boldsymbol{\eta} \sim \mathcal{N}(\mathbf{0}, \mathbf{I}). \quad (19)$$

In practice, we set $k = 0$.

Token-aligned history fusion. In addition to conditioning through \mathbf{c} , we add a lightweight *additive* boundary cue to the model’s input tokens. Concretely, at any flow time t (including $t = 0$ with $\mathbf{z}_t = \mathbf{z}_0$), we form the token embeddings from \mathbf{z}_t and then add an aligned history term:

$$\text{Tok}(\mathbf{z}_t)(k, n) \leftarrow \text{Tok}(\mathbf{z}_t)(k, n) + \alpha g_k \left(\mathbf{b}(n) + \omega_k \mathbf{d}(n) \right), \quad (20)$$

where $\text{Tok}(\cdot)$ denotes the model input tokenization, α is a learnable scalar, and $g_k \in (0, 1)$ is an optional learnable per-step gate. Let $\mathbf{z}(-2, n)$ denote the second last history latent slice. The

boundary feature $\mathbf{b}(n)$ and velocity hint $\mathbf{d}(n)$ are computed from the last history steps at the *same* spatial token n :

$$\mathbf{b}(n) = \text{Tok}(\mathbf{z}(-1, n)), \quad \mathbf{d}(n) = \text{Tok}(\mathbf{z}(-1, n)) - \text{Tok}(\mathbf{z}(-2, n)), \quad (21)$$

and ω_k linearly increases from 0 (first future step) to 1 (last future step), so the fusion progressively extends the cue deeper into the future horizon.

E.2 Camera Movement Caption Dataset Augmentation

To enrich text conditioning with explicit camera cues, we augment MagicData captions with short camera-motion phrases estimated from the extracted point tracks. For each clip, we robustly estimate global camera translation from track displacements and further decompose residual motion into radial (zoom) and tangential (roll) components around the image center; remaining residual jitter is summarized as a handheld/shake score. We then map these statistics to a small vocabulary of camera primitives (e.g., pan/tilt, zoom in/out, static/handheld) with coarse speed buckets, and append the resulting phrase to the original caption during training.

E.3 Visibility Predictor

As an auxiliary component, we predict token-level visibility for the generated future motion, since points may become occluded or leave the image. Given future latent tokens $\mathbf{z}^f \in \mathbb{R}^{T \times N \times C}$, we train a lightweight predictor f_ω that outputs per-token visibility logits $\ell \in \mathbb{R}^{T \times N}$.

The predictor is applied independently to each spatial token. For each token, we first apply a linear projection to the C -dimensional features, then use a short stack of 1D temporal convolutions along the latent-time axis, and finally apply a 1×1 projection to produce one logit per latent time step. For supervision, we downsample the dense future visibility mask \mathbf{M}^f to the TrajLoom-VAE token grid using max-pooling (equivalently, a logical OR) to obtain token-level targets. We optimize a binary cross-entropy loss with logits.

At inference time, we run f_ω on generated future latents $\hat{\mathbf{z}}^f$ and threshold $\sigma(\ell)$ to obtain predicted visibility $\hat{\mathbf{m}}^f$. This visibility head is lightweight and independent of the trajectory generator.